

Tunnel Valley Current Filter in the Partially Overlapped Graphene under the Vertical Electric Field

Ryo Tamura

Faculty of Engineering, Shizuoka University, 3-5-1 Johoku, Hamamatsu 432-8561, Japan

The tunnel current (TC) and valley current (VC) are crucial in realizing high-speed and energy-saving in next-generation devices. This paper presents the TC and VC link in the partially overlapped graphene. Under the vertical electric field, the two graphene layers have the opposite AB sublattice symmetry, followed by a block on the intravalley transmission. In the allowed intervalley transmission, the difference in the phase of the decay factor prefers only one of the valleys in the output according to the overlapped length. These results suggest that the band gap with no edge state is a new platform of valleytronics.

The tunnel current (TC) and valley current (VC) are clues to satisfy the demand for high-speed and energy-saving devices. The magnetic tunnel junction serves many applications in the random access memory and hard disk drive.¹⁾ The pure VC unaccompanied by a charge current is expected to be dissipationless.^{2,3)} However, the TC and VC linkage has yet to be a primary target in these fields. The term 'valley' is a synonym of the inequivalent valence band minimums well separated in the reciprocal space. Graphene⁴⁻⁶⁾ and transition metal dichalcogenide (TMD)⁷⁾ are typical valleytronics materials that possess two inequivalent corner points, K_+ and K_- , in the Brillouin zone. A critical issue is the control of the VC, $J_+ - J_-$, where J_+ and J_- denote the contributions of valleys K_+ and K_- , respectively, to the charge current $J_+ + J_-$. A basic unit is a junction with the transmission rate $T_{v',v}$ from the K_v to $K_{v'}$ valley. Based on the Landauer-Büttiker formula (LBF), $T_{\pm} = \sum_{v'} T_{\pm,v'}$ is contribution of the K_{\pm} valley to the conductance $(2e^2/h)(T_+ + T_-)$. When $T_v \gg T_{-v}$, the junction works as the VC filter (VCF) that generates the K_v -polarized VC from the valley-unpolarized current. The VCF emerges from the line defect,⁸⁻¹¹⁾ the strain field,¹²⁻¹⁸⁾ zigzag edge states,^{19,20)} and gate voltage.^{21,22)} When $T_{+,-} + T_{-,+} \gg T_{+,+} + T_{-,-}$, the junction indicates the VC reversal (VCR). The VCR is expected to appear in the zigzag ribbons,²³⁾ $\sqrt{3} \times \sqrt{3}$ superlattice,²⁴⁻²⁶⁾ and partially overlapped graphene (po-G).^{27,28)}

The circularly polarized light²⁹⁻³²⁾ and the gate voltage³³⁾ lift the valley degeneracy in the

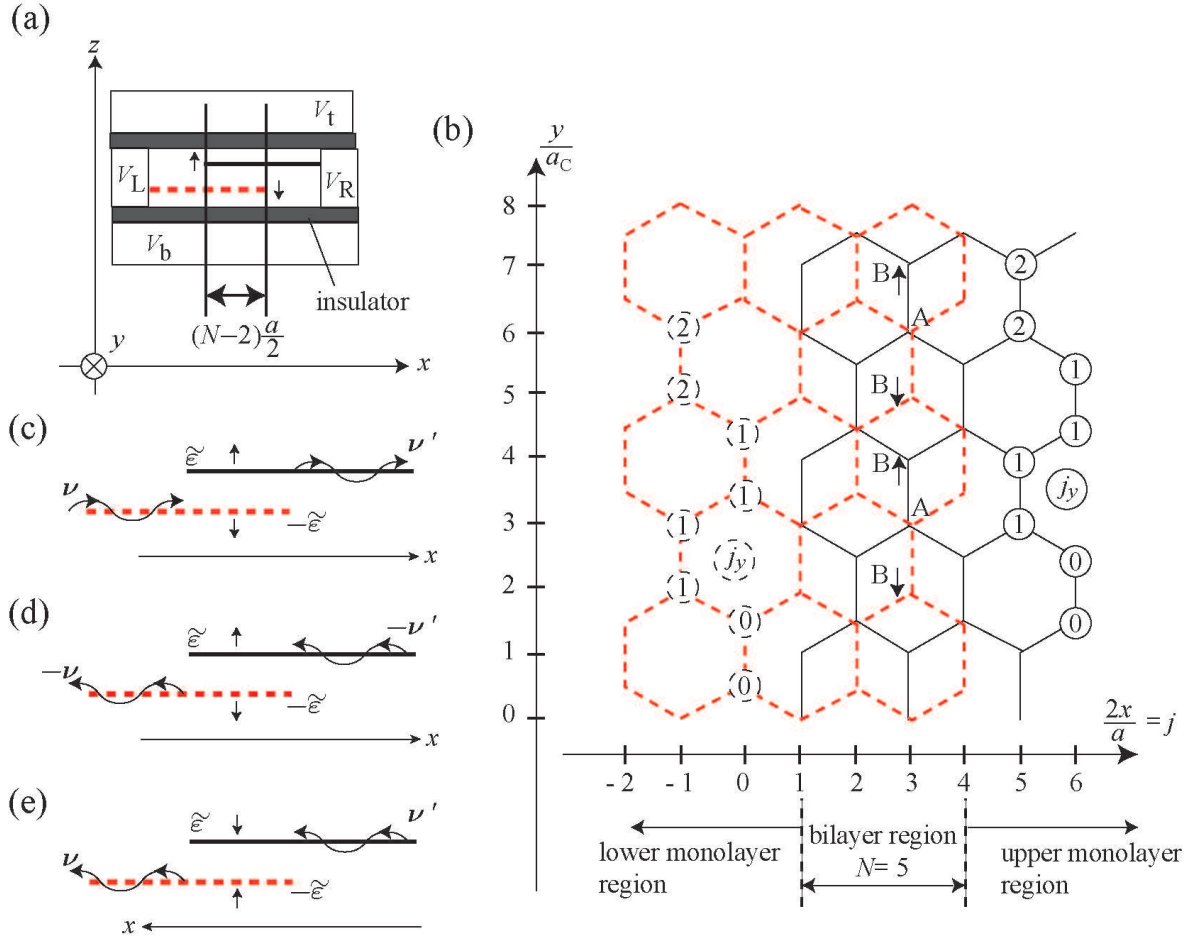


Fig. 1. (a) Side view of the partially overlapped graphene (po-G). (b) Site labels, j , j_y , A , B , \downarrow , and \uparrow in the case of $N = 5$. (c),(d),(f) Wavy arrows represent the probability flow. Refer to the main text.

TMD junction under the magnetic proximity effect, followed by intervalley difference in the energy band. When the bulk K_V band overlaps the K_{-V} band gap at the Fermi level, the band gap blocks the K_{-V} current, and the K_V -polarized VCF emerges. In the proper sense, this is *not* a tunnel junction because the extended K_V states carry the VC. In contrast, the TMD-based VCF in Ref.³⁴⁾ is an actual tunnel junction because only the evanescent states mediate the VC in the band gap. In contrast to the intrinsic gap of the TMD, a nonzero band gap requires the vertical electric fields in the bilayer^{35–40)} and substrate effects in the monolayer.^{41–43)} This may be why the TC-VCF has never been discussed in the graphene system. This paper proposes the TC-VCF in the po-G shown in Fig. 1(a). There are many works in the LBF conductance of po-G,^{44–52)} but the VC is discussed only in Refs.^{27,28)}. The top V_t and bottom V_b gate electrodes exert the vertical electric field and induce the band gap in the overlapped region. Unlike the TMD junction in Ref.,³⁴⁾ this TC-VCF does not require the magnetic field. Under

the setup of source V_L and drain V_R electrodes, the tunnel electrons inevitably pass along the interlayer paths. Side-contacted armchair nanotubes (sc-ANT) are similar to the po-G, where the intertube difference in the doping strength corresponds to the vertical electric field. The VCF and VCR simultaneously occur at the gap center of the sc-ANT.⁵³⁾ Although the VCR of the po-G was analyzed for the outside of the energy gap,^{27,28)} the TC-VCF of the po-G remains unsettled. When the Fermi level is in the band gap, the edge states⁵⁴⁾ and the whole valence band⁵⁵⁾ were theoretically predicted to carry the VC. This paper shows that the TC is the third possibility.

Figure 1(b) illustrates the atomic structures of the po-G. The dotted and solid lines depict the lower (\downarrow) and upper (\uparrow) layers, respectively. Integer indexes (j, j_y) and sublattice indexes (A, B) specify the atomic coordinate (x, y) as $x = \frac{a}{2}j$, $y_{A,\downarrow} = y_{A,\uparrow} = 3a_c[j_y + \frac{1+(-1)^j}{4}]$, $y_{B,\downarrow} = y_A - a_c$ and $y_{B,\uparrow} = y_A + a_c$ with the lattice constant a and the bond length $a_c = a/\sqrt{3}$. $(N-2)a/2$ denotes the geometrical overlap length with an integer N . The bilayer region is limited to $1 \leq j \leq N-1$. According to Ref.,⁵⁶⁾ the TB parameters are $\gamma_0 = -3.12$ eV, $\gamma_1 = 0.377$ eV, $\gamma_3 = 0.29$ eV, $\gamma_4 = 0.12$ eV with the standard notation.⁵⁷⁾ The interlayer site energy difference 2ε represents the vertical electric field; the site energies are $-\varepsilon$ and $+\varepsilon$ in the \downarrow and \uparrow layers, respectively. In this paper, we choose $\varepsilon = 0.35$ eV, which opens the band gap in the energy region $|E| < 0.17$ eV. The comparable band gap was induced in the dual gate experiment.³⁷⁾ Applying the exact method of Ref.⁵⁸⁾ with the periodic boundary condition for the y direction, we can calculate $T_{\nu,\nu}(k_y)$ that denotes the transmission rate with a transverse wave number k_y . The LBF conductance is $(2e^2/h)(2M+1)\langle T_{\text{all}} \rangle$ with the k_y average

$$\langle \diamond \rangle = \frac{1}{2M+1} \sum_{m=-M}^M \diamond(m\Delta k_y) \quad (1)$$

and the valley index sum

$$T_{\text{all}} = T_+ + T_-, \quad T_{\pm} = T_{\pm,+} + T_{\pm,-}, \quad (2)$$

where $\Delta k_y = \frac{2\pi}{3N_y a_c}$, and the integer N_y stands for the transverse width $3N_y a_c$. In the exact calculation of this paper, $N_y = 1000$. The integer M denotes the maximum effective k_y in the unit of Δk_y . Because of the monolayer dispersion relation, $\sin^2(3k_y a_c/2) \leq (E \pm \varepsilon)^2/\gamma_0^2$, and M is close to $N_y||E| - |\varepsilon|/|\pi\gamma_0|$. Figure 2(a) shows the exact VCF polarity $\langle T_+ - T_- \rangle / \langle T_{\text{all}} \rangle$ as a function of N for the six energies, $E = \pm 0.02, \pm 0.06, \pm 0.1$ eV. All the six energies are in the band gap. The data are classified according to the remainder of N divided by three, denoted by $\text{mod}(N)$. Circles, x marks, and squares correspond to the data of $\text{mod}(N) = 0, 1$, and 2, respectively. As E approaches the gap center ($E = 0$), the decay factor of the wave

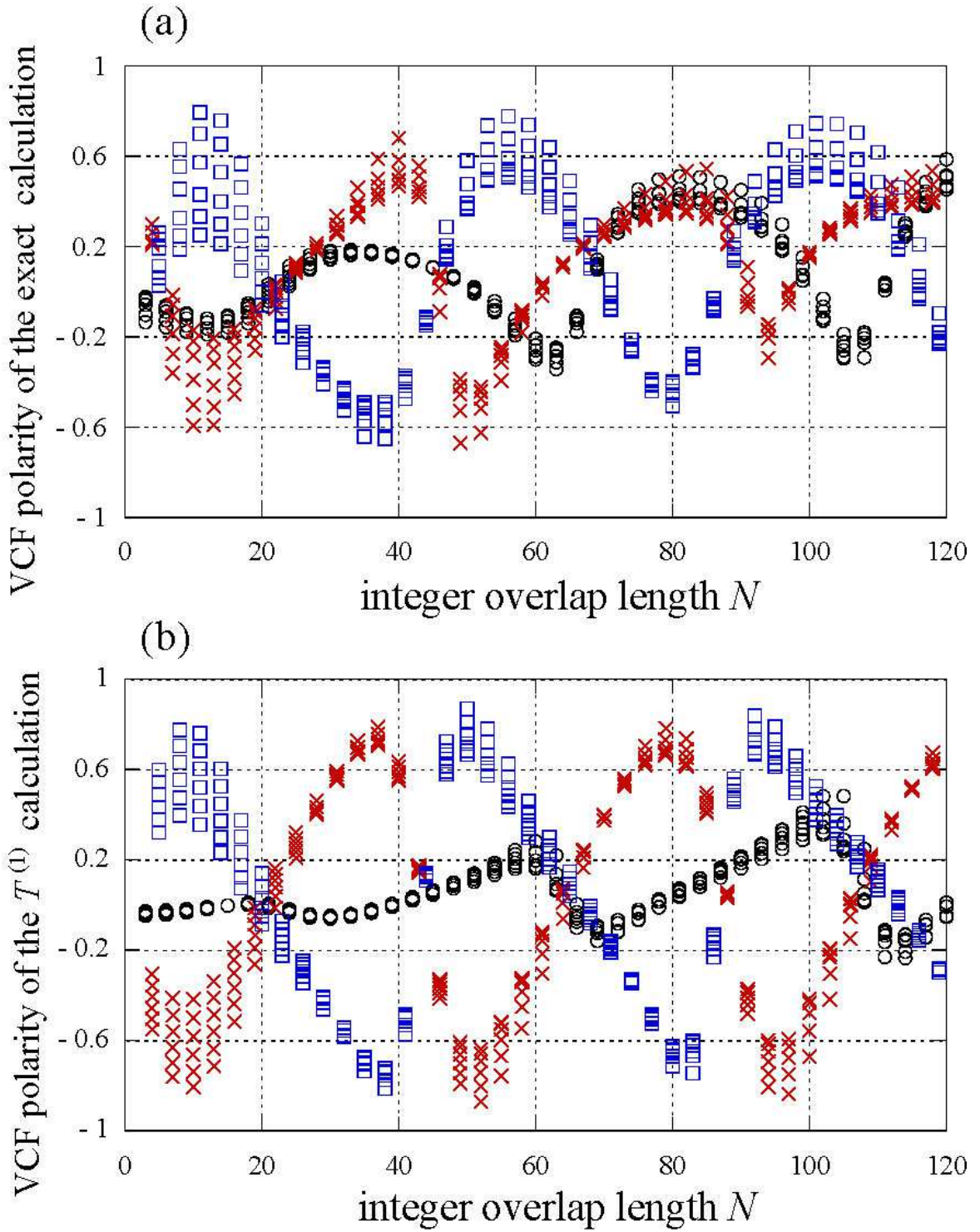


Fig. 2. VCF polarity in the case of $\varepsilon = 0.35$ eV, and $E = \pm 0.02, \pm 0.06, \pm 0.1$ eV. Circles, x marks and squares correspond to the data of $\text{mod}(N) = 0, 1$, and 2 , respectively, where $\text{mod}(N)$ denotes the remainder of N divided by three. (a) The exact VCF polarity $\langle T_+ - T_- \rangle / \langle T_{\text{all}} \rangle$ in the case of $N_y = 1000$. (b) The approximate VCF polarity $(T_+^{(1)} - T_-^{(1)}) / T_{\text{all}}^{(1)}$.

function decreases, whereas the channel number $2M + 1$ increases. However, the small energy dependence in Fig. 2(a) suggests that these two effects are irrelevant to the ratio $\langle T_v \rangle / \langle T_{\text{all}} \rangle$.

The effective k_y range is narrow as $|k_y| < \Delta k_y M \simeq 2||E| - |\varepsilon| / (3a_c |\gamma_0|)$. According to Ref.,⁵⁸⁾ the effects of γ_3 and γ_4 are minor. Based on these observations, we calculate the transmission rate $T_{v',v}^{(1)}$ under the condition $k_y = 0, \gamma_3 = \gamma_4 = 0$, where the other parameters are the same as the exact calculation. The $T^{(1)}$ calculation is the analytic continuation of the analytic formula in Ref.²⁸⁾ In the $T^{(1)}$ calculation, the wave function in the bilayer region is represented by

$$\begin{pmatrix} \vec{c}_{\downarrow,j} \\ \vec{c}_{\uparrow,j} \end{pmatrix} = \sum_{\sigma=\pm} \sum_{l=\pm} \sum_{p=\pm} \lambda_{\sigma,l}^{p,j} \eta_{\sigma,l}^{(p)} \begin{pmatrix} \vec{d}_{\sigma,l}^{\downarrow} \\ \vec{d}_{\sigma,l}^{\uparrow} \end{pmatrix}, \quad (3)$$

where η denotes the mode amplitude. The vector

$$\left[{}^t \vec{d}_{\sigma,l}^{\downarrow}, {}^t \vec{d}_{\sigma,l}^{\uparrow} \right] = \left[(\sigma l \alpha_l, 1), \beta_l \left(\sigma l \alpha_l \frac{E - \varepsilon}{E + \varepsilon}, 1 \right) \right], \quad (4)$$

is the (σ, l) mode wave function at $j = 0$ sites, where

$$\alpha_l = \frac{E + \varepsilon}{\sqrt{P + lQ}}, \quad \beta_l = \frac{2\varepsilon E - lQ}{\gamma_1(E - \varepsilon)}, \quad (5)$$

and

$$P = E^2 + \varepsilon^2, \quad Q = i \sqrt{\gamma_1^2 \varepsilon^2 - (\gamma_1^2 + 4\varepsilon^2) E^2}. \quad (6)$$

In Eq. (3), we use notation ${}^t \vec{c}_{\xi,j} = (A_{\xi,j,0}, B_{\xi,j,0})$. $A_{\xi,j,j}$ and $B_{\xi,j,j}$ stand for the wave functions at sublattices A and B with layer index $\xi = \downarrow, \uparrow$. As $k_y = 0$ in the $T^{(1)}$ calculation, the wave functions are independent of j_y . The decay factor $\lambda_{\sigma,l}$ is

$$\lambda_{\sigma,l} = \mu_{\sigma,l} + \sqrt{\mu_{\sigma,l}^2 - 1}, \quad (7)$$

where $|\lambda_{\sigma,l}| < 1$, $\lambda_{-\sigma,-l} = \lambda_{\sigma,l}^*$, and

$$\mu_{\sigma,l} = \frac{-1}{2} \left(1 + \frac{l\sigma}{|\gamma_0|} \sqrt{P + lQ} \right). \quad (8)$$

As $\lambda_{\sigma,l} \simeq |\lambda_{\sigma,l}| e^{\sigma i 2\pi/3}$, σ represents the valley index in the bilayer region.⁵⁹⁾ When we fix the valley σ and decay direction p , there remain two degenerate evanescent modes that are complex conjugate to each other. The index l corresponds to this degeneracy, where $\alpha_- = \alpha_+^*$, and $\beta_- = \beta_+^*$. In the left monolayer region ($j \leq 0$), the wave function is approximated by

$$\vec{c}_{\downarrow,j}^{(0)} = \sum_{v=\pm} \sum_{p=\pm} e^{ipv\frac{2}{3}\pi j} \eta_{v,L}^{(p)} \begin{pmatrix} v \\ 1 \end{pmatrix}. \quad (9)$$

The scattering matrix at the boundary $j = 0$ is defined by

$$\begin{pmatrix} \vec{\eta}^{(+)} \\ \vec{\eta}_L^{(-)} \end{pmatrix} = \begin{pmatrix} r_\downarrow & t_\downarrow \\ \tilde{t}_\downarrow & \tilde{r}_\downarrow \end{pmatrix} \begin{pmatrix} \vec{\eta}^{(-)} \\ \vec{\eta}_L^{(+)} \end{pmatrix}, \quad (10)$$

where ${}^t\vec{\eta}^{(p)} = (\eta_{+,+}^{(p)}, \eta_{-,+}^{(p)}, \eta_{+,-}^{(p)}, \eta_{-,-}^{(p)})$, and ${}^t\vec{\eta}_L^{(p)} = (\eta_{+,L}^{(p)}, \eta_{-,L}^{(p)})$. Applying Eqs. (3) and (9) to the boundary conditions $\vec{c}_{\downarrow,0} = \vec{c}_{\downarrow,0}^{(0)}$, $\vec{c}_{\uparrow,0} = 0$, and $\vec{c}_{\downarrow,1} = \vec{c}_{\downarrow,1}^{(0)}$ with the approximation $\lambda_{\sigma,l} \simeq e^{i\sigma\frac{2}{3}\pi}$, we obtain

$$\begin{pmatrix} r_\downarrow & t_\downarrow \\ \tilde{t}_\downarrow & \tilde{r}_\downarrow \end{pmatrix} = \frac{2}{c_B} \begin{pmatrix} \frac{\alpha_+^2}{v_+} & \frac{-\alpha_+\alpha_-}{v_+} & \frac{\alpha_+}{v_+} \\ \frac{-\alpha_-\alpha_+}{v_-} & \frac{\alpha_-^2}{v_-} & \frac{-\alpha_-}{v_-} \\ \alpha_+ & -\alpha_- & 1 \end{pmatrix} \otimes u_B \\ + \frac{2}{c_A} \begin{pmatrix} \frac{1}{v_+} & \frac{1}{v_+} & \frac{1}{v_+} \\ \frac{1}{v_-} & \frac{1}{v_-} & \frac{1}{v_-} \\ 1 & 1 & 1 \end{pmatrix} \otimes u_A - \mathbf{1}_6, \quad (11)$$

where $\mathbf{1}_n$ is the n dimensional unit matrix, \otimes stands for the Kronecker product,

$$v_l = \frac{\alpha_l}{\beta_{(-l)}} (\beta_- - \beta_+), \quad (12)$$

$$u_A = \frac{1}{2} \begin{pmatrix} 1 & \pm 1 \\ \pm 1 & 1 \end{pmatrix}, \quad c_A = 1 + \frac{\alpha_+^{\pm 1}\beta_- + \alpha_-^{\pm 1}\beta_+}{\beta_- - \beta_+}. \quad (13)$$

Indexes B and A in Eqs. (11) correspond to the periodic sublattice localization discussed in Ref.²⁸⁾. The probability flow is determined by $\eta_{\sigma,l}$, $\lambda_{\sigma,l}$, $\eta_{\sigma,l}^{(p)}$, and v_l .⁶⁰⁾ The 6×6 matrix of Eq. (10) is not unitary, but $\tilde{r}_\downarrow^* \tilde{r}_\downarrow = \mathbf{1}_2$, corresponding to the perfect reflection in the case of infinite N . We also obtain an approximate formula

$$\begin{pmatrix} r_\uparrow & t_\uparrow \\ \tilde{t}_\uparrow & \tilde{r}_\uparrow \end{pmatrix} = \frac{1}{V} \otimes \mathbf{1}_2 \begin{pmatrix} r'_\downarrow & t'_\downarrow \\ \tilde{t}'_\downarrow & \tilde{r}'_\downarrow \end{pmatrix} V \otimes \mathbf{1}_2, \quad (14)$$

for the scattering at the boundary $j = N$, where V is the 3×3 diagonal matrix with the elements $V_{1,1} = \beta_1$, $V_{2,2} = \beta_2$, and $V_{3,3} = 1$. We transform $r_\downarrow, t_\downarrow, \tilde{r}_\downarrow, \tilde{t}_\downarrow$, into $r'_\downarrow, t'_\downarrow, \tilde{r}'_\downarrow, \tilde{t}'_\downarrow$, by replacing (α_l, β_l) with $(\alpha'_l, \beta'_l) = \left(\frac{E-\varepsilon}{E+\varepsilon}\alpha_l, \frac{1}{\beta_l}\right)$. Combining Eqs. (11) and (14), we derive the approximate transmission rate $T_{\nu',\nu}^{(1)} = |t_{\nu',\nu}^{(1)}|^2$ where

$$t^{(1)} = \tilde{t}_\uparrow \Lambda^N (\mathbf{1}_4 - r_\downarrow \Lambda^N r_\uparrow \Lambda^N)^{-1} t_\downarrow \quad (15)$$

and Λ is the diagonal matrix with the elements defined by Eq. (7).

Figure 2(b) shows the approximate VCF polarity $(T_+^{(1)} - T_-^{(1)})/T_{\text{all}}^{(1)}$. The decaying factor $\lambda_{\sigma,l}$ is not a real number, and thus causes the periodic oscillation, reproducing the oscillation of

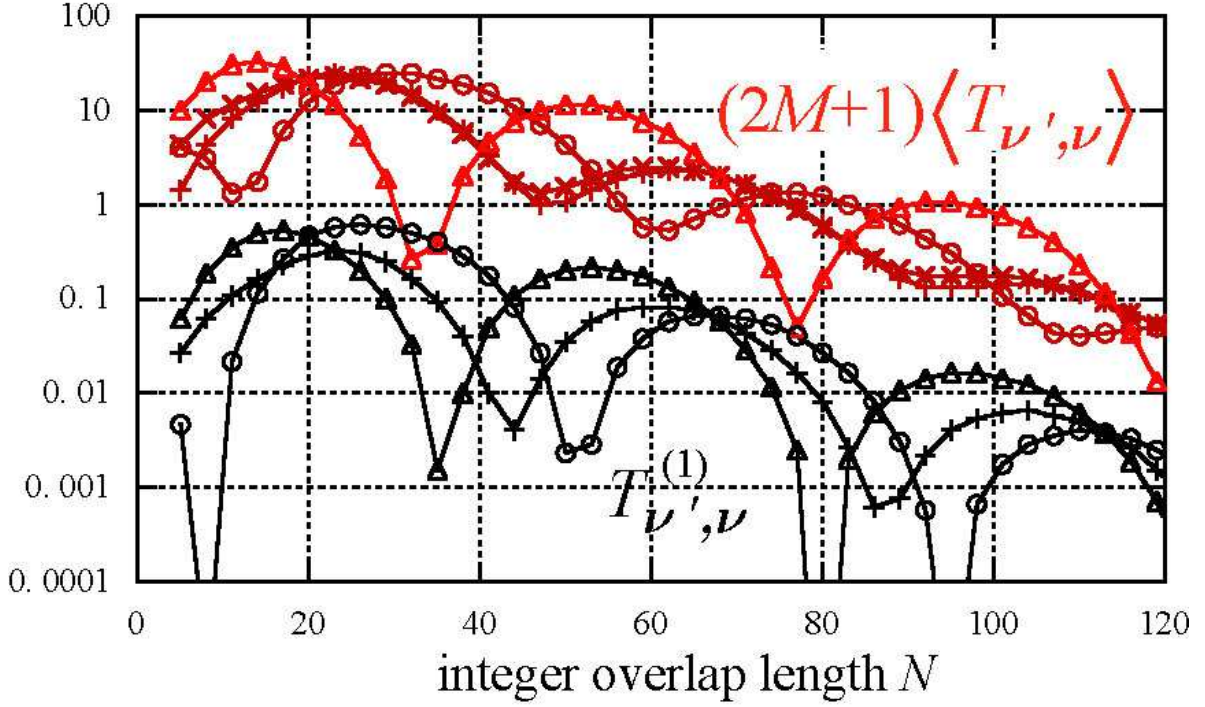


Fig. 3. Exact VC components $(2M+1)\langle T_{\nu',\nu} \rangle$ (red symbols) and the approximate transmission rate $T_{\nu',\nu}^{(1)}$ (black symbols) in the case of $\text{mod}(N) = 2$, $\varepsilon = 0.35$ eV, $E = 0$, and $N_y = 1000$. Under these conditions, $M = 35$. The triangles, circles, + and x marks represent the cases $(\nu', \nu) = (+, -), (-, +), (+, +)$, and $(-, -)$, respectively, where ν' and ν correspond to the valleys of the output and input flows, respectively. Since $T_{+,+}^{(1)} = T_{-,-}^{(1)}$ holds at the zero E , we omit the black x marks.

the Fig. 2(a) as follows. The K_+ (K_-) peak appears when $N \simeq 37$, and 79 ($N \simeq 10, 52$, and 97) in the case of $\text{mod}(N) = 1$. Compared with this case, the VCF polarity is opposite and small in the case of $\text{mod}(N) = 2$ and 1, respectively. Figure 3 displays the valley-resolved components of the square data in Fig. 2. Red and black symbols in Fig. 3 represent the $(2M+1)\langle T_{\nu',\nu} \rangle$ and $T_{\nu',\nu}^{(1)}$, respectively, under the conditions of $\text{mod}(N) = 2$, $E = 0$, $\varepsilon = 0.35$ eV, and $N_y = 1000$. The E , ε and N_y determine that $M = 35$. Since the energy dependence is small in Fig. 2, we mainly discuss the zero E . The triangles, circles, + and x marks represent the cases $(\nu', \nu) = (+, -), (-, +), (+, +)$, and $(-, -)$, respectively. Since $T_{+,+}^{(1)} = T_{-,-}^{(1)}$ at the zero E , we omit the black x marks. Owing to the narrow effective k_y range, $T_{\nu',\nu}^{(1)}$ reproduces the essential characteristics of $\langle T_{\nu',\nu} \rangle$ as in the relation between Figs. 2(a) and 2(b). Considering the periodic boundary condition, we neglect the edge mode.^{19,20,23} This assumption is reasonable under the following conditions. The number of the right-going zigzag edge modes is only one per valley in the gap center.⁶¹ In the case of $N < 60$, the edge mode has little influence on the VGR polarity in Fig. 2 because the corresponding values of $(2M+1)|\langle T_+ - T_- \rangle|$ are much

larger than one in Fig. 3. Interestingly, the VCF and VCR simultaneously appear in Fig. 3. The K_ν -polarized VCF occurs when $T_{\nu,-\nu} > T_{-\nu,\nu}$. Contrarily, the intravalley transmission is irrelevant to the VCF as $T_{+,+} \simeq T_{-,-}$. Notably, the relation $\langle T_{\nu',\nu} \rangle = \langle T_{\nu,\nu'} \rangle$ does *not* hold. Here, we fix the notation $\langle T_{\nu',\nu}(E, \varepsilon) \rangle$ according to the three rules; (1) The left and right subindexes represent the valleys of the transmitted and incident waves, respectively. (2) The direction of the x axis is the same as that of the incident wave. (3) The layer with the incident (transmitted) wave is labeled by \downarrow (\uparrow) and has the site energy $-\varepsilon$ ($+\varepsilon$). Figure 1(c) represents the incident and transmitted waves corresponding to $\langle T_{\nu',\nu}(E, \bar{\varepsilon}) \rangle$. The complex conjugate operation (CCO) of the wave function transforms Fig. 1(c) into Fig. 1(d) and Fig. 1(e), where the rules (2) and (3) are not applied to Fig. 1(d) for the comparison. First, The CCO causes reversal both in the probability flow and in the valley. This results in the change of the subindex from (ν', ν) to $(-\nu, -\nu')$ according to the rule (1). Second, the rule (2) causes the inversion of the x axis, accompanied by the change $(-\nu, -\nu') \rightarrow (\nu, \nu')$. Lastly, the rule (3) changes the assignment of \downarrow and \uparrow , and thus $\varepsilon = -\bar{\varepsilon}$ in Fig. 1(e). Comparing Fig. 1(c) with Fig. 1(e), we prove

$$\langle T_{\nu',\nu}(E, \varepsilon) \rangle = \langle T_{\nu,\nu'}(E, -\varepsilon) \rangle \quad (16)$$

and find that $\langle T_{\nu,\nu'} \rangle \neq \langle T_{\nu',\nu} \rangle$ with a nonzero ε . With the transformation $(A'_\downarrow, B'_\downarrow) = (A_\downarrow^*, -B_\downarrow^*)$ and $(A'_\uparrow, B'_\uparrow) = (-A_\uparrow^*, B_\uparrow^*)$, we can also prove

$$T_{\nu',\nu}^{(1)}(E, \varepsilon) = T_{-\nu',-\nu}^{(1)}(-E, -\varepsilon). \quad (17)$$

Because of Eqs. (16) and (17), $T_{+,+} \simeq T_{-,-}$ holds when $E \simeq 0$.

When N is large and E is close to zero, $T_{\nu',\nu}^{(1)}$ is approximated by $T_{\nu',\nu}^{(2)} = |t_{\nu',\nu}^{(2)}|^2$, where

$$\begin{aligned} t_{\nu',\nu}^{(2)} &= (\tilde{t}_\uparrow \Lambda^N t_\downarrow)_{\nu',\nu}|_{E=0} \\ &= \frac{1}{i} \text{Re} \left[\left(\frac{\alpha_0}{|\tilde{c}_B|^2} - \frac{\nu\nu'}{\alpha_0|\tilde{c}_A|^2} \right) (\tilde{\lambda}_+^N + \tilde{\lambda}_-^N) \right] \\ &\quad + \frac{1}{i} \left(\frac{\nu}{\tilde{c}_B^* \tilde{c}_A} - \frac{\nu'}{\tilde{c}_A^* \tilde{c}_B} \right) \text{Re}[\tilde{\lambda}_+^N - \tilde{\lambda}_-^N], \end{aligned} \quad (18)$$

α_0 , \tilde{c}_B , \tilde{c}_A , and $\tilde{\lambda}_\pm$ stand for $\alpha_{+,+}$, c_B , c_A , and $\lambda_{\pm,+}$, respectively, in the case of zero E ; $\alpha_0 = \varepsilon / \sqrt{\varepsilon^2 + i|\varepsilon|\gamma_1}$, $\tilde{c}_B = 1 + (\alpha_0 - \alpha_0^*)/2$, $\tilde{c}_A = 1 + (\alpha_0^* - \alpha_0)/(2|\alpha_0|^2)$, $\tilde{\lambda}_\pm = \mu_\pm + \sqrt{\mu_\pm^2 - 1}$, and $\mu_\pm = -\frac{1}{2} \mp \frac{\varepsilon}{2|\gamma_0|\alpha_0}$. For an intuitive picture of Eq. (18), we define the wave function matching $I_{\nu',\nu}$ as

$$I_{\nu',\nu} \equiv \frac{1}{2i} \sum_{\sigma,l} \beta_l^{-1} \lambda_{\sigma,l}^N(\nu', 1) \vec{d}_{\sigma,l}^\uparrow(\nu, 1) \vec{d}_{\sigma,l}^\downarrow. \quad (19)$$

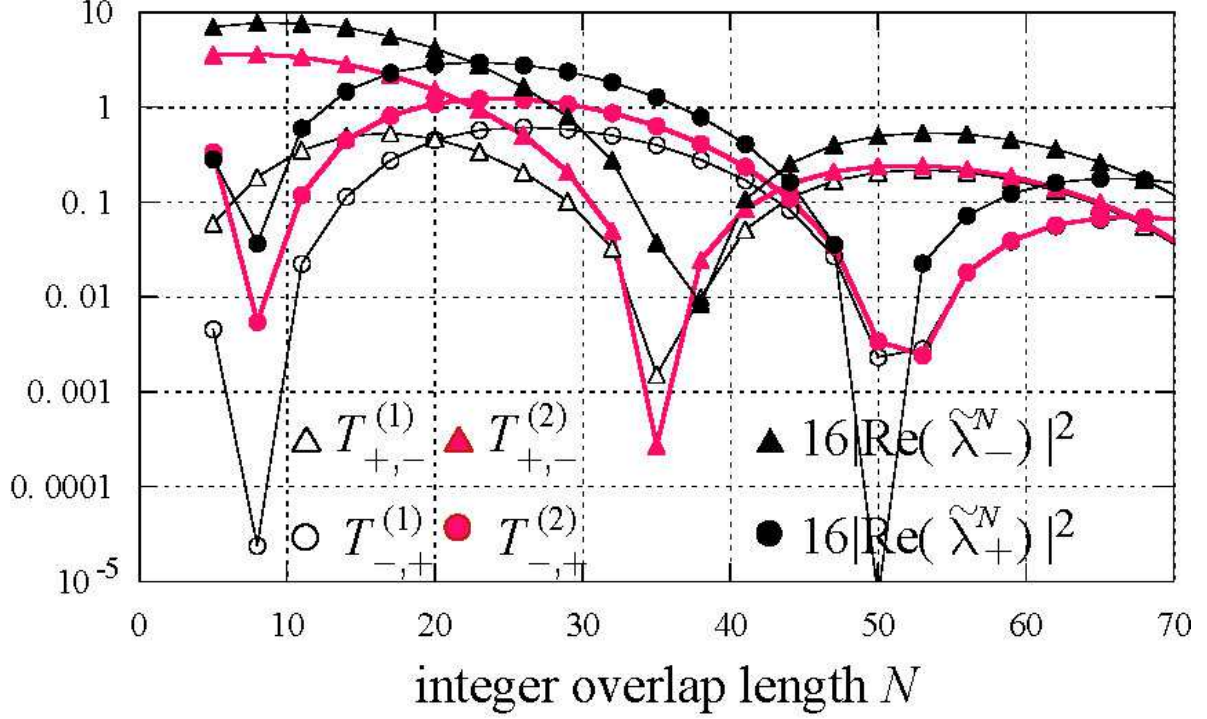


Fig. 4. The approximate intervalley transmission rates, $T_{\pm, \mp}^{(1)}$, $T_{\pm, \mp}^{(2)}$, and $16|\text{Re}(\tilde{\lambda}_{\pm}^N)|^2$, in the case of $\varepsilon = 0.35$ eV, $E = 0$, and $\text{mod}(N) = 2$.

The factors $(\nu', 1)\vec{d}_{\sigma, l}^{\uparrow}\lambda_{\sigma, l}^N$ and $(\nu, 1)\vec{d}_{\sigma, l}^{\downarrow}$ correspond to the transmission at $j = 0$ and $j = N$, respectively. We choose the coefficient $1/(2i\beta_l)$ to obtain the relation

$$\lim_{\frac{\varepsilon}{\gamma_1} \rightarrow \pm\infty} t_{\nu', \nu}^{(2)} = \lim_{\frac{\varepsilon}{\gamma_1} \rightarrow \pm\infty} I_{\nu', \nu}|_{E=0} \quad (20)$$

$$= \frac{4}{i}\delta_{\nu', -\nu}\text{Re}\left(\tilde{\lambda}_{\nu \frac{\varepsilon}{|\varepsilon|}}^N\right). \quad (21)$$

In Fig. 4, $T_{-, \nu}^{(1)}$ data in Fig. 3 are compared with the $T_{-, \nu}^{(2)}$ and $16|\text{Re}(\tilde{\lambda}_{\pm}^N)|^2$. $T^{(2)}$ reproduces $T^{(1)}$, especially when $N > 30$. Although the ε is slightly smaller than the γ_1 , the factor $|\text{Re}(\tilde{\lambda}_{\pm}^N)|^2$ qualitatively explains the oscillation, contrasting with the monotonic decay caused by the factor $|\tilde{\lambda}|^{2N}$. When the sign of ε is reversed, the VCF polarity is also reversed, similar to other gated graphene systems.^{9, 11, 19, 20} In the case of Eq. (20), the factor $(E - \varepsilon)/(E + \varepsilon) = -1$ in $(\nu', 1)\vec{d}_{\sigma, l}^{\uparrow}$ blocks the intravalley ($\nu' = \nu$) transmission. Additionally, the factors $(\nu, 1)\vec{d}_{\sigma, l}^{\downarrow*}$ and $(-\nu, 1)\vec{d}_{\sigma, l}^{\uparrow}$, which correspond to the VCR ($\nu' = -\nu$), simultaneously grow in Eq. (20) under the condition of $\nu\sigma\varepsilon/|\varepsilon| = 1$, leading us to Eq. (21).

The TC-VCF and TC-VCR have been ignored in the graphene system. Given the successful application of tunneling magnetoresistance, the TC deserves to be surveyed.¹⁾ Moreover, we can measure the tunneling time^{62, 63)} in the band gap using optical measurement. The

pump polarized pulse light is shed on the left monolayer, creating a high population in the K_v valley.⁶⁴⁻⁶⁹ This high population drives the K_v electrons to diffuse to the valley-unpopulated area, i.e., to the right monolayer. The probe pulse light illuminates the right monolayer region and induces the second harmonic generation (SHG).^{69,70} The SHG signal of the K_v valley corresponds to the VCR and thus is a signature of the TC. The delay time of the probe light gives us the time scale information. The absolute value of the decay factor is close to one and permits a significant variation in the tunnel barrier thickness. Under the condition $(2M + 1)\langle T_{\pm, \mp} \rangle \gg 1$ in Fig. 3, the thickness reaches about 15 nm, indicating that the po-G is a new platform for exploring the tunneling process.

References

- 1) A. Fert, *Rev. Mod. Phys.* **80**, 1517 (2008).
- 2) S. A. Vitale, D. Nezich, J. O. Varghese, P. Kim, N. Gedik, P. Jarillo-Herrero, D. Xiao, and M. Rothschild, *Small* **14**, 1801483 (2018).
- 3) M. Yamamoto, Y. Shimazaki, I. V. Borzenets, and S. Tarucha, *J. Phys. Soc. Jpn* **84**, 121006 (2015).
- 4) N. M. R. Peres, *Rev. Mod. Phys.* **82**, 2673 (2010).
- 5) S. Das Sarma, S. Adam, E. H. Hwang, and E. Rossi, *Rev. Mod. Phys.* **83**, 407 (2011).
- 6) A. H. Castro Neto, F. Guinea, N. M. R. Peres, K. S. Novoselov, and A. K. Geim, *Rev. Mod. Phys.* **81**, 109 (2009).
- 7) G. Wang, A. Chernikov, M. M. Glazov, T. F. Heinz, X. Marie, T. Amand, and B. Urbaszek, *Rev. Mod. Phys.* **90**, 021001 (2018).
- 8) Y. Liu, J. Song, Y. Li, Y. Liu, and Q. F. Sun, *Phys. Rev. B* **87**, 195445 (2013).
- 9) J.-H. Chen, G. Autes, N. Alem, F. Gargiulo, A. Gautam, M. Linck, C. Kisielowski, O. V. Yazyev, S. G. Louie, and A. Zettl, *Phys. Rev. B* **89**, 121407(R) (2014).
- 10) D. Gunlycke and C. T. White, *Phys. Rev. Lett.* **106**, 136806 (2011).
- 11) V. H. Nguyen, S. Dechamps, P. Dollfus, and J.-C. Charlier, *Phys. Rev. Lett.* **117**, 247702 (2016).
- 12) M. Settnes, S. R. Power, M. Brandbyge, and A-P. Jauho, *Phys. Rev. Lett.* **117**, 276801 (2016).
- 13) A. Chaves, L. Covaci, K. Y. Rakhimov, G. A. Farias, and F. M. Peeters, *Phys. Rev. B* **82**, 205430 (2010).
- 14) L. S. Cavalcante, A. Chaves, D. R. da Costa, G. A. Farias, and F. M. Peeters, *Phys. Rev. B* **94**, 075432 (2016).
- 15) T. Fujita, M. B. A. Jalil, and S. G. Tan, *Appl. Phys. Lett.* **97**, 043508 (2010).
- 16) F. Zhai, X. Zhao, K. Chang, and H. Q. Xu, *Phys. Rev. B*, **82**, 115442 (2010).
- 17) C.-C Hsu, M. L. Teague, J.-Q Wang, and N.-C Yeh, *Sci. Adv.* **6**, eaat9488 (2020).
- 18) W. Ortiz, N. Szpak, and T. Stegmann, *Phys. Rev. B* **106**, 035416 (2022).
- 19) A. Rycerz, J. Tworzydło, and C. W. J. Beenakker *Nat. Phys.* **3**, 172 (2007).
- 20) H. Santos, L. Chico, and L. Brey, *Phys. Rev. Lett.* **103**, 086801 (2009).

- 21) J. L. Garcia-Pomar, A. Cortijo, and M. Nieto-Vesperinas, *Phys. Rev. Lett.* **100**, 236801 (2008).
- 22) H. Schomerus, *Phys. Rev. B* **82**, 165409 (2010).
- 23) A. R. Akhmerov, J. H. Bardarson, A. Rycerz, C. W. J. Beenakker, *Phys. Rev. B* **77**, 205416 (2008).
- 24) S. K. Wang and J. Wang, *Phys. Rev. B* **92**, 075419 (2015).
- 25) J. J. Wang, S. Liu, J. Wang, and J. -F. Liu, *Phys. Rev. B* **98**, 195436 (2018).
- 26) C. W. J. Beenakker, N. V. Gnezdilov, E. Dresselhaus, V. P. Ostroukh, Y. Herasymenko, I. Adagideli, and J. Tworzydło, *Phys. Rev. B* **97**, 241403(R) (2018).
- 27) R. Li, Z. Lin, and K. S. Chan, *Physica E* **113**, 109 (2019).
- 28) R. Tamura, arXiv:2301.10978, *J. Phys. Soc. Jpn.* in press.
- 29) X.-J. Qiu, Z.-Z. Cao, J. Hou, and C.-Y. Yang, *Appl. Phys. Lett.* **117**, 102401 (2020).
- 30) Y. Hajati, M. Alipourzadeh, and I. Makhfudz, *Phys. Rev. B* **103**, 245435 (2021).
- 31) D. Liu, B. Liu, R. Yuan, J. Zheng, and Y. Guo, *Phys. Rev. B* **103**, 245432 (2021).
- 32) L. Luo, S. Wang, J. Zheng, and Y. Guo, *Phys. Rev. B* **108**, 075434 (2023).
- 33) M. Tahir, P. M. Krstajić, and P. Vasilopoulos, *Phys. Rev. B* **95**, 235402 (2017).
- 34) D. Szcześniak and S. Kais, *Phys. Rev. B* **101**, 115423 (2020).
- 35) Y. Shimazaki, M. Yamamoto, I. V. Borzenets, K. Watanabe, T. Taniguchi, and S. Tarucha, *Nature Phys.* **11**, 1032 (2015).
- 36) M. Sui, G. Chen, L. Ma, W. -Y. Shan, D. Tian, K. Watanabe, T. Taniguchi, X. Jin, W. Yao, D. Xiao, and Y. Zhang, *Nature Phys.* **11**, 1027 (2015).
- 37) J. Yin, C. Tan, D. Barcons-Ruiz, I. Torre, K. Watanabe, T. Taniguchi, J. C. W. Song, J. Hone, and F. H. L. Koppens, *Science* **375**, 1398 (2022).
- 38) E. McCann, *Phys. Rev. B* **74**, 161403(R) (2006).
- 39) J. Nilsson, A. H. C. Neto, F. Guinea, and N. M. R. Peres, *Phys. Rev. B* **78**, 045405 (2008).
- 40) Y. Zhang, T. T. Tang, C. Girit, Z. Hao, M. C. Martin, A. Zettl, M. F. Crommie, Y. R. Shen and F. Wang, *Nature* **459**, 820 (2009).
- 41) R. V. Gorbachev, J. C. W. Song, G. L. Yu, A. V. Kretinin, F. Withers, Y. Cao, A. Mishchenko, I. V. Grigorieva, K. S. Novoselov, L. S. Levitov, and A. K. Geim, *Science* **346**, 448 (2014).

- 42) K. Komatsu, Y. Morita, E. Watanabe, D. Tsuya, K. Watanabe, T. Taniguchi, and S. Moriyama, *Sci. Adv.* **4**, eaaq0194 (2018).
- 43) J. H. J. Martiny, K. Kaasbjerg, and A. -P. Jauho, *Phys. Rev. B* **100**, 155414 (2019).
- 44) E. Cannavò, D. Marian, E. G. Marín, G. Iannaccone, and G. Fior, *Phys. Rev. B* **104**, 085433 (2021).
- 45) H. Z. Olyaei, P. Ribeiro, and E. V. Castro, *Phys. Rev. B* **99**, 205436 (2019).
- 46) C. J. Páez, A. L. C. Pereira, J. N. B. Rodrigues, N. M. R. Peres, *Phys. Rev. B* **92**, 045426 (2015).
- 47) D. Yin, W. Liu, X. Li, L. Geng, X. Wang, and P. Huai, *Appl. Phys. Lett.* **103**, 173519 (2013).
- 48) J. Zheng, P. Guo, Z. Ren, Z. Jiang, J. Bai, Z. Zhang, *Appl. Phys. Lett.* **101**, 083101 (2012).
- 49) K. M. M. Habib, F. Zahid, R. K. Lake, *Appl. Phys. Lett.* **98**, 192112 (2011).
- 50) J. W. González, H. Santos, E. Prada, L. Brey, and L. Chico, *Phys. Rev. B* **83**, 205402 (2011).
- 51) X.-G. Li, I.-H. Chu, X. G. Zhang, and H.-P. Cheng, *Phys. Rev. B* **91**, 195442 (2015).
- 52) J. W. González, H. Santos H, M. Pacheco M, L. Chico L, and L. Brey, *Phys. Rev. B* **81**, 195406 (2010).
- 53) R. Tamura, *J. Phys. Soc. Jpn.* **90**, 114701 (2021); **92**, 038001 (2023).
- 54) J. M. Marmolejo-Tejada, J. H. Garcia, M. D. Petrović, P. -H, Chang, X. -L, . Sheng, A, Cresti, P, Plecháč, S, Roche, and B. K. Nikolić, *J. Phys. Mater.* **1**, 015006 (2018).
- 55) Y. D. Lensky, J. C. W. Song, P. Samutpraphoot, and L. S. Levitov, *Phys. Rev. Lett.* **114**, 256601 (2015).
- 56) B. Partoens and F. M. Peeters, *Phys. Rev. B* **74**, 075404 (2006).
- 57) The sign of γ_0 and γ_4 are reversed compared to Ref.⁵⁶⁾ by the transformation $(A', B') = (A, -B)$.
- 58) R. Tamura, *Phys. Rev. B* **99**, 155407 (2019).
- 59) In this paper, the square root of a complex number $X = |X|e^{i\theta}$ is defined by $\sqrt{X} = \sqrt{|X|}e^{i\frac{\theta}{2}}$ with the phase range $-\pi < \theta \leq \pi$. The real numbers Y and Z in the formula $Y + iZ = \frac{1}{|\gamma_0|} \sqrt{P + iQ}$ become positive under this range of θ . Since $|E/\gamma_0| \ll 1$ and $|\varepsilon/\gamma_0| \ll 1$, Y and Z are much less than one. Accordingly, $\mu_{\sigma,l}^2 - 1 \simeq -\frac{3}{4} + \frac{l\sigma}{2}Y + \frac{i}{2}\sigma Z$,

$$\sqrt{\mu_{\sigma,l}^2 - 1} \simeq i\frac{\sqrt{3}}{2}\left(\sigma - \frac{1}{3}Y\right), \lambda_{\sigma,l} \simeq \exp(i\sigma 2\pi/3) - \frac{l\sigma}{2}Y - \frac{i}{2}\left(\sigma Z + \frac{l}{\sqrt{3}}Y\right), \text{ and } |\lambda_{\sigma,l}|^2 \simeq 1 - \frac{\sqrt{3}}{2}Z < 1.$$

- 60) In the $T^{(1)}$ calculation, the probability flow is represented by $J = \text{Im}[\ ^t\vec{c}_{\downarrow,j}^* h \vec{c}_{\downarrow,j-1} + \ ^t\vec{c}_{\uparrow,j}^* h \vec{c}_{\uparrow,j-1}]$. Here, h denotes the Hamiltonian matrix connecting \vec{c}_j with \vec{c}_{j-1} . The elements are $h_{1,1} = h_{2,2} = 0$, and $h_{1,2} = h_{2,1} = \gamma_0$. In the $T^{(1)}$ calculation, $\gamma_3 = \gamma_4 = 0$, and γ_1 does not connect \vec{c}_j with \vec{c}_{j-1} . Using Eq. (3), we can prove $J = 2\gamma_0 \sum_{\sigma,l,p} \text{Im}[\sigma v_l \lambda_{\sigma,l}^{-1} \eta_{\sigma,l}^{(p)} \eta_{-\sigma,-l}^{(-p)*}]$.
- 61) W. Yao, S. A. Yang, Q. Niu, Phys. Rev. Lett. **102**, 096801 (2009)
- 62) E. H. Hauge and J. A. Stovneng, Rev. Mod. Phys. **61**, 917 (1989).
- 63) R. Landauer and T. Martin, Rev. Mod. Phys. **66**, 217 (1994).
- 64) W. Yao, D. Xiao, and Q. Niu, Phys. Rev. B **77**, 235406 (2008).
- 65) L. -L. Chang, Q. -P. Wu, Y. -Z Li, R. -L. Zhang, M. -R. Liu, W. -Y. Li, F. -F. Liu, X. -B. Xiao, and Z. -F. Liu, Physica E **130**, 114681 (2021).
- 66) S. A. O. Motlagh, F. Nematollahi, V. Apalkov, and M. I. Stockman, Phys. Rev. B **100**, 115431 (2019).
- 67) H. K. Kelardeh, U. Saalman, J. M. Rost, Phys. Rev. Research, **4**, L022014 (2022).
- 68) L. E. Golub, S. A. Tarasenko, M. V. Entin, and L. I. Magarill, Phys. Rev. B **84**, 195408 (2011).
- 69) M. S. Mrudul, Á. Jiménez-Galán, M. Ivanov, and G. Dixit, Optica **8**, 422 (2021).
- 70) R. Zhou, T. Guo, L. Huang, and K. Ullah, Materials Today Physics **23**, 00649 (2022).